This is the peer-reviewed, final accepted version for American Mineralogist, published by the Mineralogical Society of America.
The published version is subject to change. Cite as Authors (Year) Title. American Mineralogist, in press.
DOI: https://doi.org/10.2138/am-2023-9136. http://www.minsocam.org/

Revision 1

In-situ and *ex-situ* experimental investigation on the chalcopyrite replacement in saline solution at 310-365°C and 15-25 MPa

Luying Wang[1, 2], Heping Li[2, *], Qingyou Liu[2, 3], Sen Lin[2], and Shengbin Li[2]

[1.] School of management, Guizhou University of Commerce, Guiyang, 550014, China

[2.] Key Laboratory of High-temperature and High-pressure Study of the Earth's Interior, Institute of Geochemistry, Chinese Academy of Sciences, Guiyang, 550081, China

[3.] School of Materials & Environmental Engineering, Shenzhen Polytechnic University, 518055, Shenzhen

Corresponding author: Heping Li (liheping@vip.gyig.ac.cn)

This is the peer-reviewed, final accepted version for American Mineralogist, published by the Mineralogical Society of America.
The published version is subject to change. Cite as Authors (Year) Title. American Mineralogist, in press.
DOI: https://doi.org/10.2138/am-2023-9136. http://www.minsocam.org/

Abstract

The replacement of chalcopyrite in NaCl solutions was investigated from 310 to 365°C and 15 to 25 MPa with *ex-situ* surface characterization techniques and *in-situ* electrochemical methods. The replacement products and reactions were analyzed *ex-situ* using Raman spectroscopy, scanning electron microscope (SEM) and energy dispersive X-ray spectrometer (EDS). Chalcopyrite dissolution was monitored by open circuit potential (OCP), polarization curves and electrochemical impedance spectroscopy (EIS). The *ex-situ* and *in-situ* measurements show that: (i) elevated temperature and pressure promote the oxidative dissolution of chalcopyrite by different pathways; (ii) the altered chalcopyrite surface consists of an outer layer of hematite and an inner layer of covellite; (iii) at elevated temperature, removal of more copper from chalcopyrite surface enhances chalcopyrite dissolution, and favors hematite formation over covellite in the alteration rind; and (iv) at elevated pressure, more iron ions diffuse through the passive covellite layer by point defects, promoting chalcopyrite replacement by covellite over hematite. This study provides experimental evidence on the replacement of chalcopyrite by covellite, the precipitation of hematite and the exchange of Fe/Cu ions between chalcopyrite and hydrothermal brine.

Keywords: chalcopyrite replacement; covellite; hematite; *ex-situ* surface characterization; *in-situ* electrochemical techniques

1. Introduction

This is the peer-reviewed, final accepted version for American Mineralogist, published by the Mineralogical Society of America.
The published version is subject to change. Cite as Authors (Year) Title. American Mineralogist, in press.
DOI: https://doi.org/10.2138/am-2023-9136. http://www.minsocam.org/

Chalcopyrite is one of the most ubiquitous copper bearing sulfide minerals. It mainly occurs in copper nickel sulfide deposits, porphyry copper deposits, contact metasomatic skarn copper deposits, sandstone type copper deposits, stratiform copper deposits, vein copper deposits and volcanic-hosted massive sulfide deposits (Chen et al., 2023; Duran et al., 2017; Gritsenko et al., 2022; Li et al., 2023; Suhendra et al., 2024; Syverson et al., 2017; Tivey, 2007; Zhao et al., 2021). Therefore, chalcopyrite is formed in different geo-environments from low temperature to high temperature. Due to the multi-stage mineralization, the early formed chalcopyrite in high temperature geo-environments would be altered by later high temperature hydrothermal fluids. For instance, chalcopyrite is routinely encountered in magmatic-hydrothermal systems in the shallow continental crust, such as extensive porphyry deposits, where metal-bearing brines and vapors interact with evolving magmatic fluids (Blundy et al., 2015; Graham et al., 2004; Hedenquist et al., 1994; Syverson et al., 2017). The formation of chalcopyrite also occurs along the inner wall of chimneys in seafloor hydrothermal vent deposits, where it directly contacts venting hot spring fluids (Seewald and Seyfried, 1990; Seyfried and Ding, 1993; Tivey, 2007; Tivey et al., 1995). Therefore, it is necessary to research the chalcopyrite alteration at high temperature and pressure.

Most often, mineral-fluid interaction primarily relies on traditional chemical processes, including decomposition reactions, synthesis reactions, double displacement reactions and replacement reactions. In traditional chemical processes, chemical reactions

This is the peer-reviewed, final accepted version for American Mineralogist, published by the Mineralogical Society of America.
The published version is subject to change. Cite as Authors (Year) Title. American Mineralogist, in press.
DOI: https://doi.org/10.2138/am-2023-9136. http://www.minsocam.org/

usually require contact between reactants. However, chalcopyrite is a copper sulfide with semiconductor properties (Engin et al., 2011; McMillan et al., 1982; O'Connor and Eksteen, 2020). Semiconductor materials are capable of undergoing electrochemical reactions due to their unique electronic structure that allows electrons to transition between energy bands. In electrochemical reactions, electrons are transferred from one reactant to another through a conductive medium (such as an electrolyte solution), triggering a chemical reaction. This reaction mode does not require direct contact between reactants. As chalcopyrite is a semiconductor, both traditional chemical processes and electrochemical processes can occur on its surface. Recent studies indicate that chalcopyrite can be oxidized to bornite, covellite and element sulfur by electrochemical processes in different systems at ambient temperature and pressure through reactions (1), (2) and (3) (Almeida et al., 2016; Ghahremaninezhad et al., 2010; Liu et al., 2018). There are few studies focusing on the electrochemical oxidation of chalcopyrite at high temperature and pressure.

$$5CuFeS_2 \rightarrow Cu_5FeS_4 + 6S^0 + 4Fe^{3+} + 12e^- \quad (1)$$

$$2CuFeS_2 + 13H_2O \rightarrow 0.75CuS + 1.25Cu^{2+} + 2Fe^{3+} + 3.25SO_4^{2-} + 26H^+ + 28e^- \quad (2)$$

$$CuFeS_2 \rightarrow Cu^{2+} + Fe^{3+} + 2S^0 + 5e^- \quad (3)$$

Chalcopyrite replacement in hydrothermal systems consists of electrochemical processes and traditional chemical processes (Mikhlin et al., 2004). These electrochemical reactions obtained by electrochemical techniques are helpful to explain

78 the exchange of Cu/Fe between chalcopyrite and fluids, the replacement of chalcopyrite
79 by secondary copper minerals, and the pathway of chalcopyrite replacement in
80 hydrothermal system (Chaudhari et al., 2022; Chaudhari et al., 2021).

81 The deposits characterized by alteration are sensitive to a number of physical and
82 chemical factors, such as porosity, grain size, duration of time for alteration, temperature,
83 pressure, pH, total chloride and galvanic interaction in the ore-forming solution, which
84 control the chalcopyrite oxidation rate under hydrothermal conditions (Bilenker et al.,
85 2016; Embile et al., 2018; Knight et al., 2018; Meng et al., 2021). At present, the
86 influence of temperature and pressure on chalcopyrite-fluid reaction equilibria is not well
87 constrained under hydrothermal conditions. Zhao et al. (2014) reported the replacement
88 of chalcopyrite by bornite at 200-320°C in solutions containing Cu(I) and hydrosulfide.
89 They observed that Cu and Fe contents were controlled principally by temperature, and to
90 a lesser degree by solution pH. Chaudhari et al. (2021) investigated the replacement of
91 chalcopyrite by copper sulfides in Cu-rich solutions at 180-300°C; they found that
92 covellite always formed initially, followed by high digenite, and that the replacement of
93 chalcopyrite is driven by Cu^{2+}_{tot}. Previous experimental studies of electrochemically
94 driven chalcopyrite dissolution rarely focus on the effects of high temperature and
95 pressure, owing to several challenges encountered in performing the experiments: 1)
96 evolving solution conditions due to corrosion of the experimental apparatus; 2)
97 ineffective reference electrodes for detecting *in-situ* electrochemical behavior at high

temperature and pressure; 3) the brittleness of chalcopyrite makes it difficult to machine the working electrode into proper shapes; and 4) electrical signals are easily interfered by other electronic devices, temperature fluctuations and pressure fluctuations (Sun et al., 2009; Wang et al., 2017b). However, solutions to these challenges have recently been developed (Lin et al., 2017; Wang et al., 2017a).

This study capitalizes upon these advances to investigate the effects of temperature and pressure on the oxidative dissolution of chalcopyrite in NaCl solutions. The reactions between chalcopyrite and solution were monitored *in-situ* using OCP curves, potentiodynamic curves, and EIS, and multiple means of *ex-situ* characterization including Raman spectroscopy, scanning electron microscope (SEM), and Energy dispersive X-ray spectrometer (EDS) were used to analyze the surface products. This study provides initial constraints on the altered products of chalcopyrite in NaCl solution at elevated temperature (310 to 365°C) and pressure (15 to 25 MPa).

2. Materials and methods

2.1. Electrode preparation

The mineral chalcopyrite was collected from Shuixiexiang, Yunnan Province, China. The purity of selected chalcopyrite particles (80 - 100 mesh) was 98% as confirmed using XRD. Chalcopyrite working electrodes were prepared by high-pressure sintering selected chalcopyrite powder in a cubic multi anvil press (Wang et al., 2017a).

2.2. Experimental apparatus

Dissolution and electrochemical experiments were conducted in an autoclave system. The autoclave was equipped with a tube-type heating furnace (Shanghai Y-feng Electrical Furnace Co., Ltd., SK2-5), a temperature regulator (Xiamen Yudian Automation Technology Co., Ltd., AI-518P) and a pressure sensor (Chengdutest Electronics Co., Ltd., CY201, accuracy ±1 bar). The procedure consisted of pumping argon to the desired set pressure and heating the sample solution mixture to the desired set temperature in 3 hours. Once at the intended temperature, the temperature and pressure were kept constant until the experiment ended. The pressure was maintained at 20 MPa, when the final temperatures were 310°C, 340°C and 365°C respectively. The temperature was maintained at 340°C, when the final pressures were 15 MPa, 20 MPa and 25 MPa respectively. The target temperature and pressure were maintained at ±1°C and ±1 MPa respectively.

2.3. Surface characterization

Chalcopyrite was polished and immersed in 0.1 mol/L NaCl solutions for 3 hours in the heating process and 1 hour at the final temperature and pressure. The surface morphologies of corroded chalcopyrite samples were examined by the JSM-7800F scanning electron microscope (SEM) and the chemical compositions of oxide films were investigated using the connected Apollo XL energy-dispersive X-ray spectrometer (EDS). The compound compositions of the oxide film were determined by using Renishaw *in-Via* confocal micro-Raman spectroscopy system with a 514.5 nm argon laser excitation line.

This is the peer-reviewed, final accepted version for American Mineralogist, published by the Mineralogical Society of America.
The published version is subject to change. Cite as Authors (Year) Title. American Mineralogist, in press.
DOI: https://doi.org/10.2138/am-2023-9136. http://www.minsocam.org/

A laser power of 8 mW was used as an excitation source to avoid the further oxidation of chalcopyrite. For each acquisition, a total of 5 spectra were accumulated, each for 60 s. The spectra were collected with a CCD detector using backscattering geometry and a 50× objective lens.

2.4. Electrochemical measurements

The reference electrode was an Ag/AgCl pressure-balanced external reference electrode with 0.1 mol/L KCl reference solution, and platinum was used as a counter electrode. Considering that the reference electrode was at ambient temperature (25℃) and system pressure via the reference solution bridge, the temperature gradient between the high-temperature system and the room temperature reference electrode gave rise to a thermal diffusion potential (Sun et al., 2009). This problem has been solved by Macdonald et al. (1979), and the calibrated equation of the electrode potential is as follows:

$$\Delta E_{\mathrm{SHE}} = \Delta E_{\mathrm{obs}} + 0.2866 - 0.001\Delta T + 1.745\times10^{-7}\Delta T^2 - 3.03\times10^{-9}\Delta T^3 \quad (4)$$

where ΔE_{obs} is the observed potential of the working electrode vs. the Ag/AgCl external reference electrode, and ΔE_{SHE} is the corresponding potential vs. the standard hydrogen electrode (SHE) at the experimental temperature. $\Delta T = T - 25$℃, T is the experimental temperature.

The electrolyte was a 0.1 mol/L NaCl solution. All the electrochemical measurements were carried out in an autoclave with three electrodes as described in Lin

et al. (2017). Prior to the start of each experiment, argon was pumped into the electrolyte for 10 minutes to maintain the dissolved oxygen concentration at 0.1 ± 0.02 mg/L. Chalcopyrite was immersed in the solution at final temperature and pressure for 1 h so that the open circuit potential (OCP) was measured until it reached the 10^{-5} V/s tolerance limit. Afterward, the electrochemical impedance spectroscopy (EIS) tests - fitted by ZSimpWin 3.20 (2004) software - were performed in the frequency range of 10^{-2} Hz to 10^{4} Hz with a peak-to-peak amplitude of 10 mV. The polarization curves were plotted by changing the electrode potential automatically from –0.4 to +0.9 V versus OCP at a scan rate of 2 mV/s.

3. Results and discussion

3.1. Raman spectroscopic analysis

The altered chalcopyrite surface was characterized by Raman spectrometry. The obtained spectra are presented in Figure 1. It can be seen that the Raman vibrational peaks of leached chalcopyrite obtained at 310°C and 20 MPa are located in different wavenumber ranges compared to other samples. These frequencies were checked with the standards of covellite (CuS) and hematite (Fe_2O_3). The strong Raman vibrational peaks at ~472 cm^{-1} and in the region 1310-1338 cm^{-1} were reported as covellite and hematite respectively (Cai et al., 2012; Diliegros-Godines et al., 2019; Faria and Lopes, 2007; Urbanová et al., 2012). A mixture of covellite and hematite was detected on the chalcopyrite surface after oxidative dissolution at 310°C and 20 MPa, indicating that

hematite doesn't cover the chalcopyrite surface completely. However, in the spectrum of other samples, only hematite was detected, showing that hematite grains can cover the chalcopyrite surface at these conditions (various temperature of 340°C and 365°C at 20 MPa, and various pressure of 15 MPa, 20 MPa, and 25 MPa at 340°C). The reference data for the covellite and hematite were obtained from https://rruff.info/covellite/display=default/ and https://rruff.info/hematite/display=default/ respectively.

3.2. SEM and EDS analysis

A cross-sectional SEM study was conducted to provide further details on the characteristics of the oxide films, such as their thicknesses and morphologies. Hydrothermal dissolution of chalcopyrite resulted in the formation of three types of texture in Figure 2. A sharp boundary is observed between the inner region and the middle region. They are shown in the back-scattered electron images in different shades of gray. The medium shade of gray represents chalcopyrite. As revealed by the EDS element analysis (Table 1), the lighter shade represents the inner Cu-rich layer consisting of mainly covellite. The formation of barrier-like Cu-rich layer was attribute to the preferential leaching of iron from chalcopyrite. Then the leaching iron ions precipitated as hematite to cover the inner layer and form the outermost Fe-rich layer (the darker shade in Figure 2). It was in accordance with Raman spectrum results that the covellite and hematite were the main secondary minerals of chalcopyrite oxidization as Meng et al.

198 (2021) reported.

199 Figure 2 respectively presents the different effects of temperature (310℃, 340℃ and
200 365℃) and pressure (15 MPa, 20 MPa and 25 MPa) on the cross-sectional morphologies
201 of the chalcopyrite samples. The surface became rougher and etch pits appeared with less
202 covellite at elevated temperature. Hematite filled in the triangular pits and laid thick on
203 the chalcopyrite surface after leaching in 0.1 mol/L NaCl solutions for 1 hour at 365℃
204 (Figure 2c). At elevated pressure, the lighter region was thicker and the hematite layer
205 was more compact. When the leaching pressure was 15 MPa, hematite exhibited on the
206 chalcopyrite surface sparsely. However, when the pressure was up to 25 MPa, it became a
207 flat layer. Chalcopyrite is replaced by more covellite at elevated temperature, but less
208 covellite at elevated pressure, indicating that increasing temperature and pressure affected
209 chalcopyrite leaching by different processes.

210 **3.3. Open circuit potential**

211 Figure 3 shows the effect of temperature and pressure on the potential of the
212 chalcopyrite electrode in the 0.1 mol/L NaCl solutions after the autoclave system was
213 kept at the final temperature and pressure. The increase of temperature and pressure
214 resulted in a lower OCP. This trend suggested faster surface electrochemical reactions and
215 a less protective layer on the chalcopyrite electrode. Therefore, the elevated temperature
216 and pressure could intensify chalcopyrite dissolution. For all the samples, the steady state
217 OCP was reached as a change of less than 10^{-5} V/s before EIS and polarization curves

measurements. It was due to the spontaneous growth of stable oxide layer on the chalcopyrite surface.

3.4. Polarization curves

The polarization curves of the chalcopyrite electrode in 0.1 mol/L NaCl solution with different temperatures and pressures at a scan rate of 2 $mV \cdot s^{-1}$ were described in Figure 4. It can be seen that the increase in temperature or pressure led to an increase in the anodic current density and a decline of the corrosion potential. Chalcopyrite in the elevated temperature system had a sharp increase in corrosion density compared to the pressure variations. It was illustrated that the oxidation reaction rate of chalcopyrite increased sharply at higher temperature. At low anodic potentials (OCP to 0.05V), the pseudo-passive region was observed due to the formation of the surface layer. However, in the elevated temperature system, the pseudo-passive region disappeared, indicating the replacement of chalcopyrite by lesser amounts of covellite (Figure 4a). Conversely, in the elevated pressure system, the pseudo-passive region appeared due to more covellite was produced on the chalcopyrite surface than hematite (Figure 4b). Hence, increasing temperature and pressure promoted the oxidative dissolution of chalcopyrite by different pathways.

3.5. Electrochemical impedance spectroscopy (EIS)

EIS studies on the chalcopyrite electrodes were conducted in 0.1 mol/L NaCl solution with different temperatures and pressures. The recorded EIS spectra and

This is the peer-reviewed, final accepted version for American Mineralogist, published by the Mineralogical Society of America.
The published version is subject to change. Cite as Authors (Year) Title. American Mineralogist, in press.
DOI: https://doi.org/10.2138/am-2023-9136. http://www.minsocam.org/

corresponding fitted curves were plotted in the form of Nyquist diagrams in Figure 5. All spectra were composed of two depressed capacitive loops. The first capacitive loop at high frequencies was related to the double-layer capacitive impedance with a charge-transfer resistance. The second capacitive loop at low frequencies was attributed to the charge transfer resistance occurring within the pores of the surface layer which was considered as diffusional impedance of the oxide layer. The equivalent circuit model was shown in Figure 6 (Ghahremaninezhad et al., 2012; Tehrani et al., 2021), where R_{dl} and C_{dl} are the resistance and capacitance of the double-layer respectively. R_p and C_p are the resistance and capacitance of the passive layer respectively. The presence of the Constant Phase Angle Element (CPE) in this circuit is due to the defects in the passive layer and/or the electrode roughness.

The corresponding impedance parameters obtained at different temperatures and pressures are presented in Table 2. The double-layer resistance (R_{dl}) can be defined as follows (Bard and Faulkner, 2001; Ghahremaninezhad et al., 2012):

$$R_{dl} = \frac{RT}{nFi_0} \quad (5)$$

Where R, T, n, F and i_0 are the ideal gas constant, temperature in Kelvin, number of transferred electrons, Faraday constant and the exchange current density of the electrochemical reaction respectively. Hence, as temperatures increased from 310°C to 365°C, the R_{dl} values increased from 4.7 $\Omega \cdot cm^2$ to 173.3 $\Omega \cdot cm^2$. Increasing pressure restrained the double layer by accelerating ionic diffusion in the solution. Hence, it

reduced the number of transferred electrons in the space charge transfer region, leading to the higher R_{dl} values being monitored. The R_p values are associated with the thickness of a passive layer. CPE elements and their associated resistance depend on the point defects in the structure of the covellite layer; a thicker covellite layer contains more point defects. With increasing temperature, the R_p values decreased sharply, the R_{dl} and R_{CPE} values increased slightly, indicating that elevated temperature promoted chalcopyrite dissolution owing to less covellite forming on the chalcopyrite surface. However, with increasing pressure, the R_{CPE} values decreased sharply, the R_{dl} and R_p values increased slightly. That is, elevated temperatures and pressures affected chalcopyrite replacement by different pathways. Elevated pressure accelerated chalcopyrite dissolution by making more iron ions pass through point defects, resulting in chalcopyrite replacement by more covellite.

3.6. Effect of temperature and pressure on chalcopyrite oxidation

In the present study, chalcopyrite oxidation was investigated at the temperature range of 310-365°C and the pressure range of 15-25 MPa. Chalcopyrite is a covalent compound containing Cu^+, Fe^{3+} and mostly S^{2-} (Nigel et al., 2012; Pearce et al., 2006). More Fe^{3+} released from chalcopyrite to solution than Cu^+, leading to the precipitation of covellite on the chalcopyrite surface (reaction (2) (Ghahremaninezhad et al., 2010; Mikhlin et al., 2017; Nava and González, 2006). The dissolved Fe^{3+} reacted with OH^- in the solution and precipitated as $Fe(OH)_3$, then decomposed to form Fe_2O_3 through reactions (6), (7) and (8) (Majzlan et al., 2004; Mu et al., 2018). Though the results of our

This is the peer-reviewed, final accepted version for American Mineralogist, published by the Mineralogical Society of America.
The published version is subject to change. Cite as Authors (Year) Title. American Mineralogist, in press.
DOI: https://doi.org/10.2138/am-2023-9136. http://www.minsocam.org/

study could also be predicted and demonstrated by the calculations of chalcopyrite oxidative behavior (Garrels and Christ, 1965), this study shows precisely the chalcopyrite dissolution at the temperature range of 310-365°C and the pressure range of 15-25 MPa. The chalcopyrite surface was parted into two layers, and the outermost hematite precipitation and the inner covellite replacement products were detected after these main electrochemical reactions occurred during chalcopyrite dissolution (Figure 1 and 2). The hematite layer did not exhibit protective properties due to the presence of large pores separating the hematite particles. Therefore, the passive layer was composed of covellite.

$$2H_2O + O_2 + 4e^- \rightarrow 4OH^- \quad (6)$$

$$Fe^{3+} + 3OH^- \rightarrow Fe(OH)_3\downarrow \quad (7)$$

$$2Fe(OH)_3 \rightarrow Fe_2O_3 + 3H_2O \quad (8)$$

Elevated temperature and pressure play a crucial role in the oxidation processes of chalcopyrite. Firstly, they affect the mineral oxidation reactions. Secondly, they influence the rate these reactions take place. Lastly, they are significant in the formation of replacement minerals. It is clear that increasing temperature and pressure effectively promotes the oxidative dissolution of chalcopyrite by different pathways. In the present study, the *ex-situ* surface characterization measurements were utilized to obtain the reaction pathways of chalcopyrite dissolution together with *in-situ* electrochemical techniques, which improves the effectiveness and accuracy of experimental results. At elevated temperature, chalcopyrite is replaced by less covellite, which means more Cu^+

This is the peer-reviewed, final accepted version for American Mineralogist, published by the Mineralogical Society of America.
The published version is subject to change. Cite as Authors (Year) Title. American Mineralogist, in press.
DOI: https://doi.org/10.2138/am-2023-9136. http://www.minsocam.org/

298 release from chalcopyrite. The results may be due to the formation of more Cu^+ complex
299 $CuCl^0$, $CuCl_2^-$, $CuCl_3^{2-}$ through reactions (9), (10) and (11) (Lin et al., 1991; Lundström,
300 2009). Less passive covellite would result in further chalcopyrite dissolution. However, at
301 elevated pressure, the chalcopyrite dissolution is promoted by different pathways. Higher
302 pressure could make more iron ions diffuse through the passive covellite layer by point
303 defects to reach the passive layer/electrolyte interface. Hence, though chalcopyrite is
304 replaced by more covellite, the chalcopyrite oxidation is still stimulated.

305 $$Cu^{2+} + Cl^- + e^- \rightarrow CuCl^0 \quad (9)$$

306 $$Cu^{2+} + 2Cl^- + e^- \rightarrow CuCl_2^- \quad (10)$$

307 $$Cu^{2+} + 3Cl^- + e^- \rightarrow CuCl_3^{2-} \quad (11)$$

308 ## 4. Implications for hydrometallurgical and geological applications

309 The *ex-situ* and *in-situ* experiments on the replacement of chalcopyrite by Cu
310 sulfides provide new insights into the mineral replacement reactions in geological
311 systems. For minerals with semiconductor properties, such as chalcopyrite, pyrite, galena,
312 sphalerite and so on, electrochemical processes should also be considered as part of the
313 fluid-mineral interaction (Chen et al., 2015; Flores-Álvarez et al., 2017; Karimi et al.,
314 2017; Liu et al., 2021; Moslemi and Gharabaghi, 2017; Osadchii et al., 2015). Our study
315 provides experimental evidence on the replacement of chalcopyrite by covellite, the
316 precipitation of hematite and the exchange of Fe/Cu ions between chalcopyrite and fluids.
317 This mineral replacement mechanism can be applied in copper deposits, where covellite

318 surrounds chalcopyrite and Fe oxides coexist with chalcopyrite. Our experimental results
319 show that temperature and pressure exert an important control on the mineralogy of
320 chalcopyrite replacement. Cu(I) preferentially forms complexes
321 $CuCl^0$, $CuCl_2^-$ and $CuCl_3^{2-}$ with chloride in chloride-rich hydrothermal fluids at elevated
322 temperature (Brugger et al., 2016; Liu and McPhail, 2005; Liu et al., 2001). However,
323 preferential dissolution of iron from chalcopyrite is accompanied by retention of copper
324 on the chalcopyrite surface at elevated pressure. Therefore, abundant replacement of
325 chalcopyrite by covellite occurs at lower temperature and higher pressure, abundant
326 precipitation of hematite happens at higher temperature and pressure in a neutral pH and
327 high salinity fluid.

328 There is a consensus view in hydrometallurgy that chalcopyrite dissolution is
329 inhibited due to the formation of a passive layer on the surface (O'Connor and Eksteen,
330 2020). These different passive layers include a metal-deficient sulfide, a metal-deficient
331 polysulfide, elemental sulfur or jarosite in different experimental conditions (Carneiro
332 and Leão, 2007; Córdoba et al., 2008; Debernardi et al., 2013; Harmer et al., 2006;
333 Klauber, 2008; Munoz et al., 1979; Parker et al., 2008; Stott et al., 2000; Wang et al.,
334 2021). Our experimental work provides an optimized strategy for the hydrometallurgy of
335 chalcopyrite. At elevated pressure, more iron ions diffuse into the solutions, leaving a
336 thicker covellite layer on the chalcopyrite surface to impede further chalcopyrite
337 dissolution. However, at elevated temperature, more copper ions dissolve from the

chalcopyrite surface to inhibit the formation of a passive covellite layer on the chalcopyrite surface. Therefore, higher temperature at ambient pressure would be further studied to enhance the hydrothermal dissolution of chalcopyrite and the release of Cu.

Acknowledgments

Sincere thanks to Shaohua Dong for help with the tests of JSM-7800F scanning electron microscopy (SEM) and the connected Apollo XL energy-dispersive X-ray spectroscopy (EDS). This work was financially supported by project of National Natural Science Foundation of China (U1812402, 41903054), the CAS "Light of West China" Program (Luying Wang 2019), Guizhou Provincial Science and Technology Projects (QKHJC-ZK[2021]YB216).

Reference

Almeida, T.d.C., Garcia, E.M., da Silva, H.W.A., Matencio, T., and Lins, V.d.F.C. (2016) Electrochemical study of chalcopyrite dissolution in sulfuric, nitric and hydrochloric acid solutions. International Journal of Mineral Processing, 149, 25-33.

Bard, A.J., and Faulkner, L.R. (2001) Electrochemical Methods, Fundamentals and Applications, 2nd ed., 833 p. John Wiley & Sons, New York.

Bilenker, L.D., Romano, G.Y., and McKibben, M.A. (2016) Kinetics of sulfide mineral oxidation in seawater: Implications for acid generation during in situ mining of seafloor hydrothermal vent deposits. Applied Geochemistry, 75, 20-31.

Blundy, J., Mavrogenes, J., Tattitch, B., Sparks, S., and Gilmer, A. (2015) Generation of porphyry copper

deposits by gas–brine reaction in volcanic arcs. Nature Geoscience, 8(3), 235-240.

Brugger, J., Liu, W., Etschmann, B., Mei, Y., Sherman, D.M., and Testemale, D. (2016) A review of the coordination chemistry of hydrothermal systems, or do coordination changes make ore deposits? Chemical Geology, 447, 219-253.

Cai, Y., Chen, X., Ding, J., and Zhou, D. (2012) Leaching mechanism for chalcopyrite in hydrochloric acid. Hydrometallurgy, 113-114, 109-118.

Carneiro, M.F.C., and Leão, V.A. (2007) The role of sodium chloride on surface properties of chalcopyrite leached with ferric sulphate. Hydrometallurgy, 87(3-4), 73-82.

Chaudhari, A., Brugger, J., Ram, R., Chowdhury, P., Etschmann, B., Guagliardo, P., Xia, F., Pring, A., Gervinskas, G., Liu, A., and Frierdich, A. (2022) Synchronous solid-state diffusion, dissolution-reprecipitation, and recrystallization leading to isotopic resetting: insights from chalcopyrite replacement by copper sulfides. Geochimica et Cosmochimica Acta, 331, 48-68.

Chaudhari, A., Webster, N.A.S., Xia, F., Frierdich, A., Ram, R., Etschmann, B., Liu, W., Wykes, J., Brand, H.E.A., and Brugger, J. (2021) Anatomy of a complex mineral replacement reaction: Role of aqueous redox, mineral nucleation, and ion transport properties revealed by an in-situ study of the replacement of chalcopyrite by copper sulfides. Chemical Geology, 581, 120390.

Chen, G., Chen, M., Ke, C., and Tang, Y. (2023) Paleozoic VMS-type stratiform mineralization overprinted by Mesozoic vein-type mineralization in the Yushui copper deposit, eastern Guangdong, South China. Ore Geology Reviews, 158, 105498.

Chen, J., Ke, B., Lan, L., and Li, Y. (2015) Influence of Ag, Sb, Bi and Zn impurities on electrochemical and flotation behaviour of galena. Minerals Engineering, 72, 10-16.

379 Córdoba, E.M., Muñoz, J.A., Blázquez, M.L., González, F., and Ballester, A. (2008) Leaching of
380 chalcopyrite with ferric ion. Part II: Effect of redox potential. Hydrometallurgy, 93(3), 88-96.
381 Debernardi, G., Gentina, J.C., Albistur, P., and Slanzi, G. (2013) Evaluation of processing options to avoid
382 the passivation of chalcopyrite. International Journal of Mineral Processing, 125, 1-4.
383 Diliegros-Godines, C.J., Lombardero-Juarez, D.I., Machorro-Mejía, R., González, R.S., and Pal, M. (2019)
384 Electrical properties and spectroscopic ellipsometry studies of covellite CuS thin films deposited
385 from non ammoniacal chemical bath. Optical Materials, 91, 147-154.
386 Duran, C.J., Barnes, S-J., Plese, P., Prasek, M.K., Zientek, M.L., and Page, P. (2017) Fractional
387 crystallization-induced variations in sulfides from the Norilsk-Talnakh mining district (polar
388 Siberia, Russia). Ore Geology Reviews, 90, 326-351.
389 Embile, R.F., Walder, I.F., Schuh, C., and Donatelli, J.L. (2018) Cu, Pb and Fe release from
390 sulfide-containing tailings in seawater: Results from laboratory simulation of submarine tailings
391 disposal. Marine Pollution Bulletin, 137, 582-592.
392 Engin, T.E., Powell, A.V., and Hull, S. (2011) A high temperature diffraction-resistance study of
393 chalcopyrite, $CuFeS_2$. Journal of Solid State Chemistry, 184(8), 2272-2277.
394 Faria, D.L.A.D., and Lopes, F.N. (2007) Heated goethite and natural hematite: Can Raman spectroscopy be
395 used to differentiate them? Vibrational Spectroscopy, 45(2), 117-121.
396 Flores-Álvarez, J.M., Elizondo-Álvarez, M.A., Dávila-Pulido, G.I., Guerrero-Flores, A.D., and Uribe-Salas,
397 A. (2017) Electrochemical behavior of galena in the presence of calcium and sulfate ions. Minerals
398 Engineering, 111, 158-166.
399 Garrels, R.M., and Chirst, C.L. (1965) Solutions, Minerals, and Equilibria, 2nd ed., 465 p. Harper and Row,

New York.

Ghahremaninezhad, A., Asselin, E., and Dixon, D.G. (2010) Electrochemical evaluation of the surface of chalcopyrite during dissolution in sulfuric acid solution. Electrochimica Acta, 55(18), 5041-5056.

Ghahremaninezhad, A., Dixon, D.G., and Asselin, E. (2012) Kinetics of the ferric–ferrous couple on anodically passivated chalcopyrite ($CuFeS_2$) electrodes. Hydrometallurgy, 125-126, 42-49.

Graham, S., Pearson, N., Jackson, S., Griffin, W., and O'Reilly, S.Y. (2004) Tracing Cu and Fe from source to porphyry: in situ determination of Cu and Fe isotope ratios in sulfides from the Grasberg Cu–Au deposit. Chemical Geology, 207(3), 147-169.

Gritsenko, Y.D., Kondrikova, A.P., Gilbricht, S., Schoneveld, L., Barnes, S.J., Godel, B.M., Sluzhenikin, S.F., Petrenko, D.B., Seifert, T., and Yudovskaya, M.A. (2022) Quantitative assessment of the relative roles of sulfide liquid collection, magmatic degassing and fluid-mediated concentration of PGE in low-sulfide ores of the Norilsk intrusions. Ore Geology Reviews, 148, 105042.

Harmer, S.L., Thomas, J.E., Fornasiero, D., and Gerson, A.R. (2006) The evolution of surface layers formed during chalcopyrite leaching. Geochimica et Cosmochimica Acta, 70(17), 4392-4402.

Hedenquist, Jeffrey, W., Lowenstern, Jacob, and Nature, B.J. (1994) The role of magmas in the formation of hydrothermal ore deposits. 370(6490), 519-519.

Karimi, S., Ghahreman, A., Rashchi, F., and Moghaddam, J. (2017) The mechanism of electrochemical dissolution of sphalerite in sulfuric acid media. Electrochimica Acta, 253, 47-58.

Klauber, C. (2008) A critical review of the surface chemistry of acidic ferric sulphate dissolution of chalcopyrite with regards to hindered dissolution. International Journal of Mineral Processing, 86(1), 1-17.

Knight, R.D., Roberts, S., and Cooper, M.J. (2018) Investigating monomineralic and polymineralic reactions during the oxidation of sulphide minerals in seawater: Implications for mining seafloor massive sulphide deposits. Applied Geochemistry, 90, 63-74.

Li, S., Gao, L., Xia, F., Chen, C., Du, X., and Arkin A. (2023) Genetic relationship between skarn and porphyry mineralization at the Saibo copper deposit, West Tianshan, NW China: Constraints from fluid inclusions, H-O-C-S-Pb isotopes, and geochronology. Ore Geology Reviews, 162, 105709.

Lin, H., Wu, X., and Rao, P. (1991) The electrowinning of copper from a cupric chloride solution. JOM, 43(8), 60-65.

Lin, S., Li, H., Xu, L., Zhang, Y., and Cui, C. (2017) A novel experimental device for electrochemical measurements in supercritical fluids up to 700°C/1000 bar and its application in the corrosion study of superalloy Inconel 740H. RSC Advances, 7(54), 33914-33920.

Liu, H., Lu, X., Zhang, L., Xiang, W., Zhu, X., Li, J., Wang, X., Lu, J., and Wang, R. (2018) Collaborative effects of Acidithiobacillus ferrooxidans and ferrous ions on the oxidation of chalcopyrite. Chemical Geology, 493, 109-120.

Liu, T., Hu, Y., Chen, N., Xue, L., Feng, C., and Ye, Y. (2021) Electrochemical investigation of the oxidation of pyrite in neutral solutions. Electrochimica Acta, 393, 139078.

Liu, W., and McPhail, D.C. (2005) Thermodynamic properties of copper chloride complexes and copper transport in magmatic-hydrothermal solutions. Chemical Geology, 221(1), 21-39.

Liu, W., McPhail, D.C., and Brugger, J. (2001) An experimental study of copper(I)-chloride and copper(I)-acetate complexing in hydrothermal solutions between 50°C and 250°C and vapor-saturated pressure. Geochimica et Cosmochimica Acta, 65(17), 2937-2948.

Lundström, M. (2009) Chalcopyrite dissolution in cupric chloride solutions, 52 p. Ph. D. thesis, Helsinki University of Technology, Helsinki.

Macdonald, D.D., Scott, A.C., and Wentrcek, P. (1979) External Reference Electrodes for Use in High Temperature Aqueous Systems. Journal of the Electrochemical Society, 126(6), 908-911.

Majzlan, J., Navrotsky, A., and Schwertmann, U. (2004) Thermodynamics of iron oxides: Part III. Enthalpies of formation and stability of ferrihydrite (~$Fe(OH)_3$), schwertmannite (~$FeO(OH)_{3/4}(SO_4)_{1/8}$), and ε-$Fe_2O_3$. Geochimica et Cosmochimica Acta, 68(5), 1049-1059.

McMillan, R.S., MacKinnon, D.J., and Dutrizac, J.E. (1982) Anodic dissolution of n-type and p-type chalcopyrite. Journal of Applied Electrochemistry, 12(6), 743-757.

Meng, X., Jin, X., Li, X., Chu, F., Zhang, W., Wang, H., Zhu, J., and Li, Z. (2021) Mineralogy and geochemistry of secondary minerals and oxyhydroxides from the Xunmei hydrothermal field, Southern Mid-Atlantic Ridge (26°S): Insights for metal mobilization during the oxidation of submarine sulfides. Marine Geology, 442, 106654-106670.

Mikhlin, Y., Nasluzov, V., Romanchenko, A., Tomashevich, Y., Shor, A., and Félix, R. (2017) Layered structure of the near-surface region of oxidized chalcopyrite ($CuFeS_2$): hard X-ray photoelectron spectroscopy, X-ray absorption spectroscopy and DFT+U studies. Physical Chemistry Chemical Physics, 19, 2749-2759.

Mikhlin, Y.L., Tomashevich, Y.V., Asanov, I.P., Okotrub, A.V., Varnek, V.A., and Vyalikh, D.V. (2004) Spectroscopic and electrochemical characterization of the surface layers of chalcopyrite ($CuFeS_2$) reacted in acidic solutions. Applied Surface Science, 225(1), 395-409.

Moslemi, H., and Gharabaghi, M. (2017) A review on electrochemical behavior of pyrite in the froth

flotation process. Journal of Industrial and Engineering Chemistry, 47, 1-18.

Mu, Y., Peng, Y., and Lauten, R.A. (2018) The galvanic interaction between chalcopyrite and pyrite in the presence of lignosulfonate-based biopolymers and its effects on flotation performance. Minerals Engineering, 122, 91-98.

Munoz, P.B., Miller, J.D., and Wadsworth, M.E. (1979) Reaction mechanism for the acid ferric sulfate leaching of chalcopyrite. Metallurgical Transactions B, 10(2), 149-158.

Nava, D., and González, I. (2006) Electrochemical characterization of chemical species formed during the electrochemical treatment of chalcopyrite in sulfuric acid. Electrochimica Acta, 51(25), 5295-5303.

Cook, N.J., Ciobanu, C.L., Brugger, J., Etschmann, B., Howard, D.L., de Jonge, M.D., Ryan, C., and Paterson, D. (2012) Determination of the oxidation state of Cu in substituted Cu-In-Fe-bearing sphalerite via μ-XANES spectroscopy. American Mineralogist, 97, 476-479.

O'Connor, G.M., and Eksteen, J.J. (2020) A critical review of the passivation and semiconductor mechanisms of chalcopyrite leaching. Minerals Engineering, 154, 106401.

Osadchii, V.O., Fedkin, M.V., and Osadchii, E.G. (2015) Electrochemical determination of the thermodynamic parameters of sphalerite, ZnS. Journal of Alloys and Compounds, 636, 368-374.

Parker, G.K., Hope, G.A., and Woods, R. (2008) Gold-enhanced Raman observation of chalcopyrite leaching. Colloids and Surfaces A: Physicochemical and Engineering Aspects, 325(3), 132-140.

Seewald, J.S., and Seyfried, W.E. (1990) The effect of temperature on metal mobility in subseafloor hydrothermal systems: constraints from basalt alteration experiments. Earth and Planetary Science Letters, 101(2), 388-403.

Seyfried, W.E., and Ding, K. (1993) The effect of redox on the relative solubilities of copper and iron in Cl-bearing aqueous fluids at elevated temperatures and pressures: An experimental study with application to subseafloor hydrothermal systems. Geochimica et Cosmochimica Acta, 57(9), 1905-1917.

Stott, M.B., Watling, H.R., Franzmann, P.D., and Sutton, D. (2000) The role of iron-hydroxy precipitates in the passivation of chalcopyrite during bioleaching. Minerals Engineering, 13(10), 1117-1127.

Suhendra, R., Takahashi, R., Agangi, A., Imai, A., Sato, H., and Setiawan N.I. (2024) Textural-compositional evolution of pyrite and metal remobilization during low-grade metamorphism of metapelite: Contribution to gold mineralization in the Luk Ulo Complex, Central Java, Indonesia. Ore Geology Reviews, 166, 105966.

Sun, H., Wu, X., and Han, E. (2009) Effects of temperature on the protective property, structure and composition of the oxide film on Alloy 625. Corrosion Science, 51(11), 2565-2572.

Syverson, D.D., Luhmann, A.J., Tan, C., Borrok, D.M., Ding, K., and Seyfried, W.E. (2017) Fe isotope fractionation between chalcopyrite and dissolved Fe during hydrothermal recrystallization: An experimental study at 350°C and 500bars. Geochimica et Cosmochimica Acta, 200, 87-109.

Tehrani, M.E.H.N., Naderi, H., and Rashchi, F. (2021) Electrochemical study and XPS analysis of chalcopyrite dissolution in sulfuric acid in the presence of ethylene glycol. Electrochimica Acta, 369, 137663.

Tivey, M.K. (2007) Generation of seafloor hydrothermal vent fluids and associated mineral deposits. Oceanography, 20, 50-65.

Tivey, M.K., Humphris, S.E., Thompson, G., Hannington, M., and Rona, P.A. (1995) Deducing patterns of

505 fluid flow and mixing within the active TAG mound using mineralogical and geochemical data.
506 Journal of Geophysical Research Atmospheres, 100(B7), 12527-12555.
507 Urbanová, M., Kupčík, J., Bezdička, P., Šubrt, J., and Pola, J. (2012) Room-temperature sulfidation of
508 copper nanoparticles with sulfur yielding covellite nanoparticles. Comptes Rendus Chimie, 15(6),
509 511-516.
510 Wang, J., Xie, L., Han, L., Wang, X., Wang, J., and Zeng, H. (2021) In-situ probing of electrochemical
511 dissolution and surface properties of chalcopyrite with implications for the dissolution kinetics and
512 passivation mechanism. Journal of Colloid and Interface Science, 584, 103-113.
513 Wang, L., Li, H., Liang, W., Yin, Y., and Liu, Q. (2017a) High pressure sintering of a pure, compact and
514 malleable chalcopyrite block. Materials Letters, 199, 61-64.
515 Wang, L., Li, H., Liu, Q., Xu, L., Lin, S., and Zheng, K. (2017b) Effect of sodium chloride on the
516 electrochemical corrosion of Inconel 625 at high temperature and pressure. Journal of Alloys and
517 Compounds, 703, 523-529.
518 Zhao, J., Brugger, J., Ngothai, Y., and Pring, A. (2014) The replacement of chalcopyrite by bornite under
519 hydrothermal conditions. American Mineralogist, 99(11-12), 2389-2397.
520 Zhao, Z., Wei, J., Liang, S., and Gao, T. (2021) Sulfide remobilization and trace element redistribution
521 during metamorphism and deformation at the Xitieshan Pb-Zn deposit, NW China. Ore Geology
522 Reviews, 136, 104170.

523
524
525

526 **Figure captions**

527 **Figure 1.** The effects of temperature and pressure on the Raman spectra of the oxide films
528 on the surface of chalcopyrite after 1 h corrosion tests in 0.1 mol/L NaCl solutions.

529 **Figure 2.** Cross-sectional SEM images of the chalcopyrite samples after leaching in 0.1
530 mol/L NaCl solutions at different temperatures and pressures. Conditions: (a-c) different
531 temperatures at 20 MPa; (d-f) different pressures at 340°C. Cpy: chalcopyrite; Cv:
532 covellite; Hem: hematite.

533 **Figure 3.** The open circuit potential of the chalcopyrite electrode in 0.1 mol/L NaCl
534 solutions at different temperatures and pressures. Conditions: (a) different temperatures at
535 20 MPa; (b) different pressures at 340°C.

536 **Figure 4.** The polarization of curves of chalcopyrite electrode in 0.1 mol/L NaCl
537 solutions at different temperatures and pressures with a scan rate of 2 mV/s. Conditions:
538 (a) different temperatures at 20 MPa; (b) different pressures at 340°C.

539 **Figure 5.** Nyquist plots of chalcopyrite electrode at OCP in 0.1 mol/L NaCl solution at
540 different temperatures and pressures. Conditions: (a) different temperatures at 20 MPa; (b)
541 different pressures at 340°C.

542 **Figure 6.** Equivalent circuit for the chalcopyrite electrode at OCP in 0.1 mol/L NaCl
543 solution at the temperatures and pressures.

544

545 **Table 1.** EDS elemental analysis of Cu-rich layer for the chalcopyrite samples in 0.1

546 mol/L NaCl solutions at different temperature and pressure conditions

Conditions		Cu (%)	Fe (%)	S (%)	O (%)
T (°C)	P (MPa)				
310		66.6	6.5	26.2	0.8
340	20	63.1	9.9	26.2	0.9
365		61.8	11.5	25.6	1.1
	15	61.2	11.3	25.4	2.0
340	20	63.1	9.9	26.2	0.9
	25	64.2	9.8	25.3	0.7

547 **Tabel 2.** Model parameters for equivalent circuit of Figure 6

Conditions		R_{dl}	R_p	R_{CPE}	χ^2
T (°C)	P (MPa)	($\Omega \cdot cm^2$)	($\Omega \cdot cm^2$)	($\Omega \cdot cm^2$)	
310		4.7	785.9	0.104	0.0090950
340	20	116.2	150.8	3.339	0.0007332
365		173.3	72.1	56.190	0.0016480
	15	30.1	114.0	452.700	0.0004080
340	20	116.2	150.8	3.339	0.0007332
	25	253.0	180.6	1.146	0.0003420

548

Figure 1

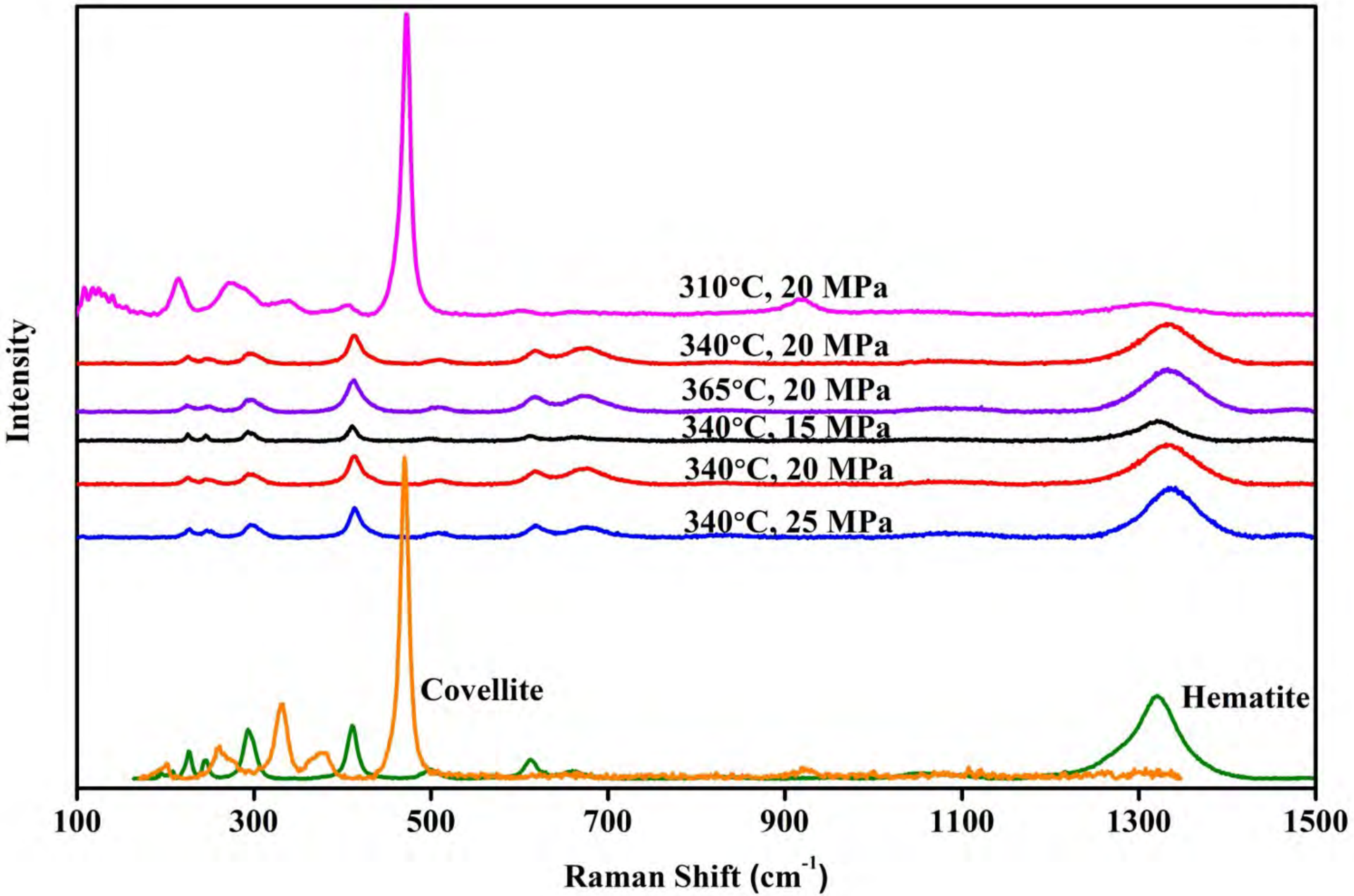
310°C, 20 MPa
340°C, 20 MPa
365°C, 20 MPa
340°C, 15 MPa
340°C, 20 MPa
340°C, 25 MPa
Covellite
Hematite
Intensity
100
300
500
700
900
1100
1300
1500
Raman Shift (cm-1)

Figure 2

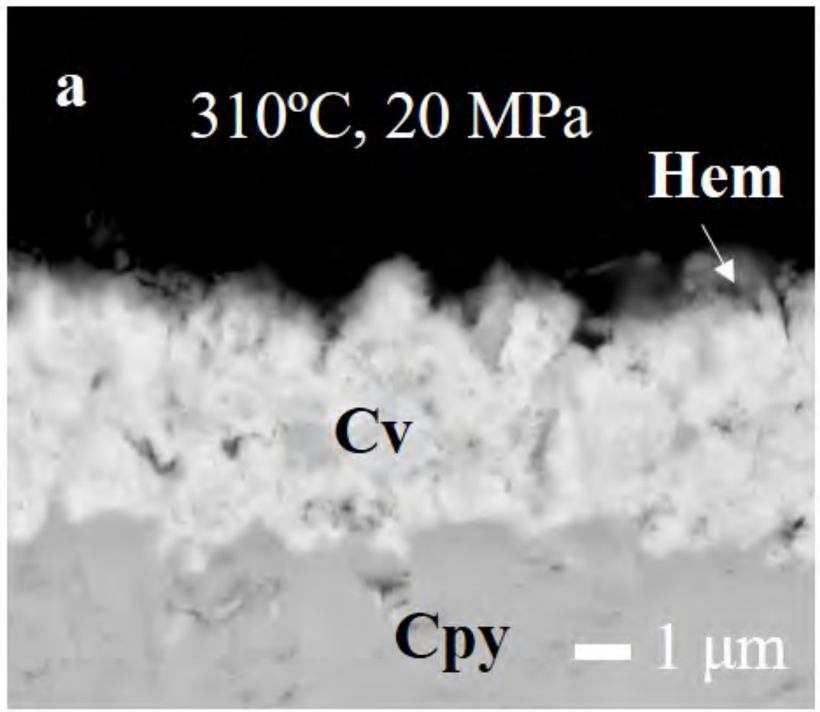
a
310ºC, 20 MPa
Hem
Cv
Cpy
1 µm

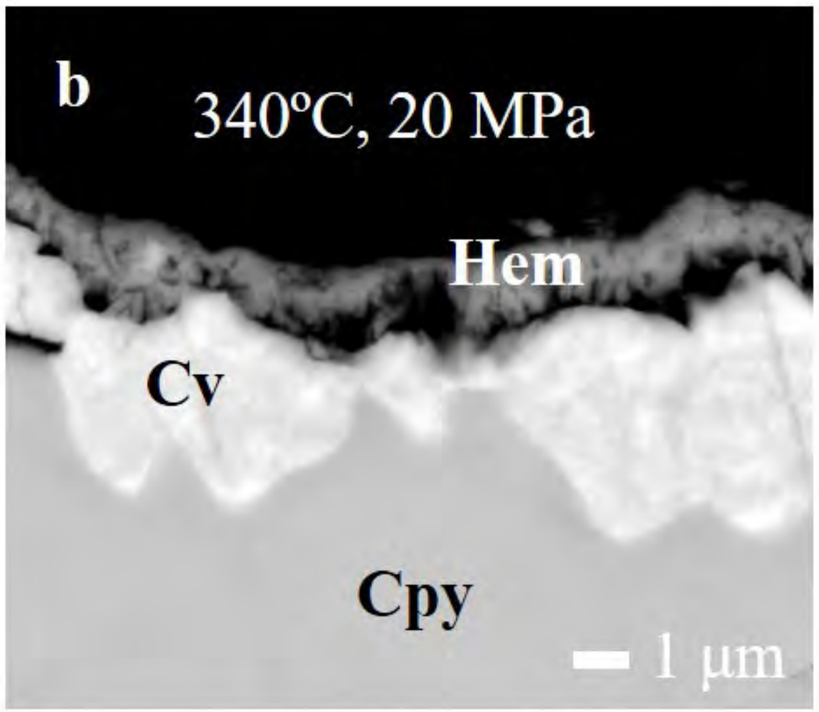
b
340ºC, 20 MPa
Hem
Cv
Cpy
1 µm

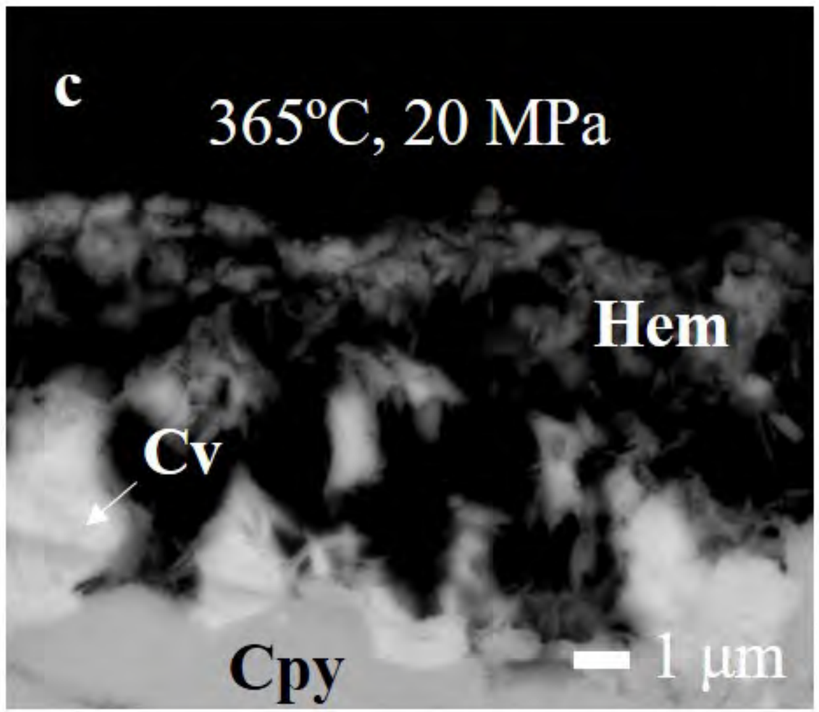
c
365ºC, 20 MPa
Hem
Cv
Cpy
1 µm

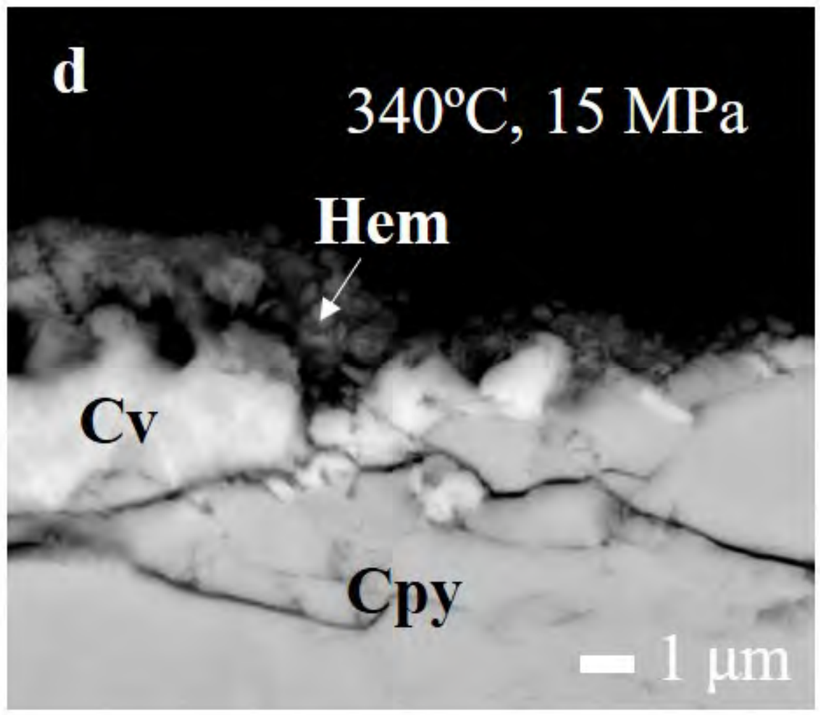
d
340ºC, 15 MPa
Hem
Cv
Cpy
1 µm

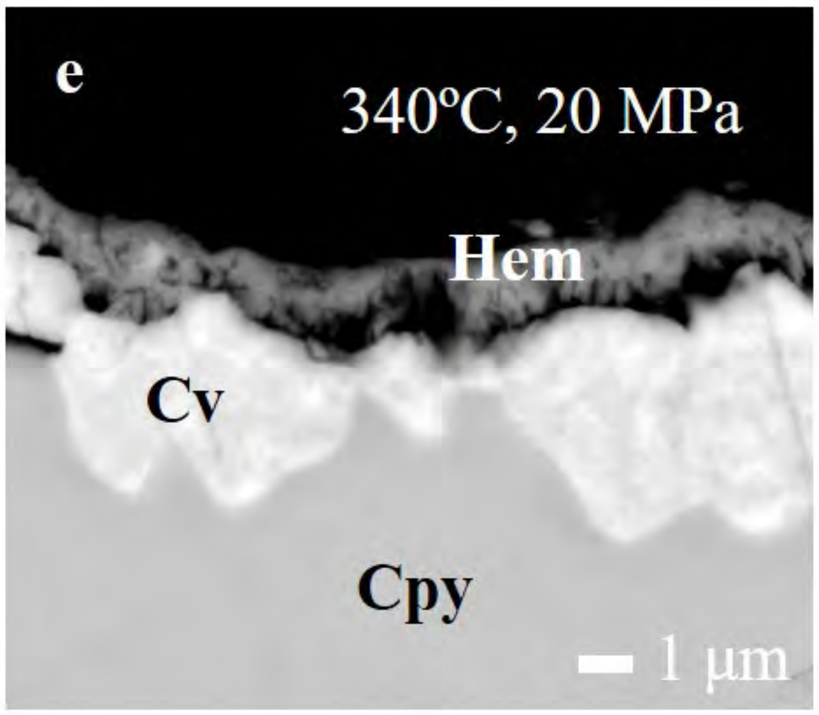
e
340ºC, 20 MPa
Hem
Cv
Cpy
1 µm

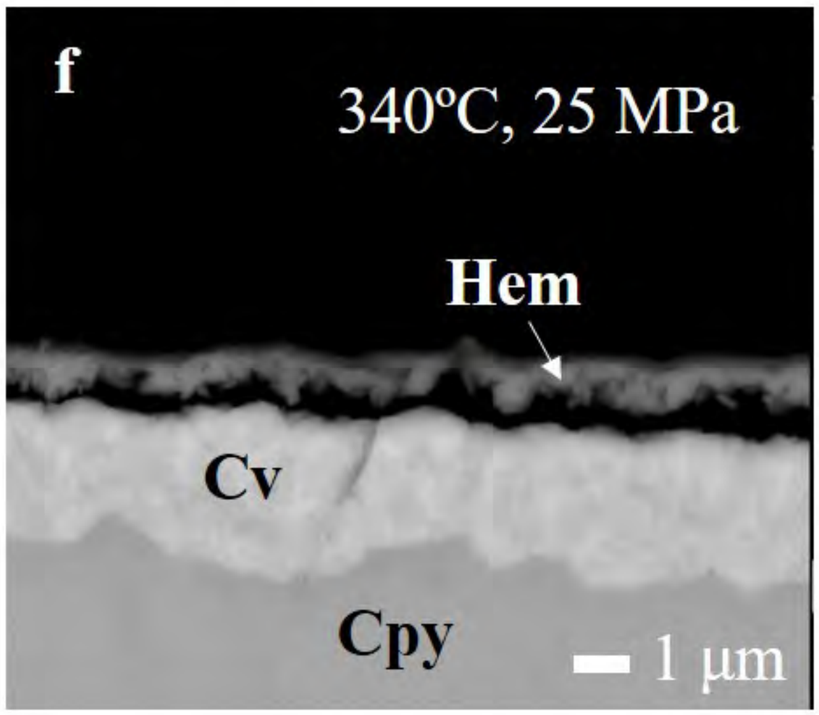
f
340ºC, 25 MPa
Hem
Cv
Cpy
1 µm

Figure 3

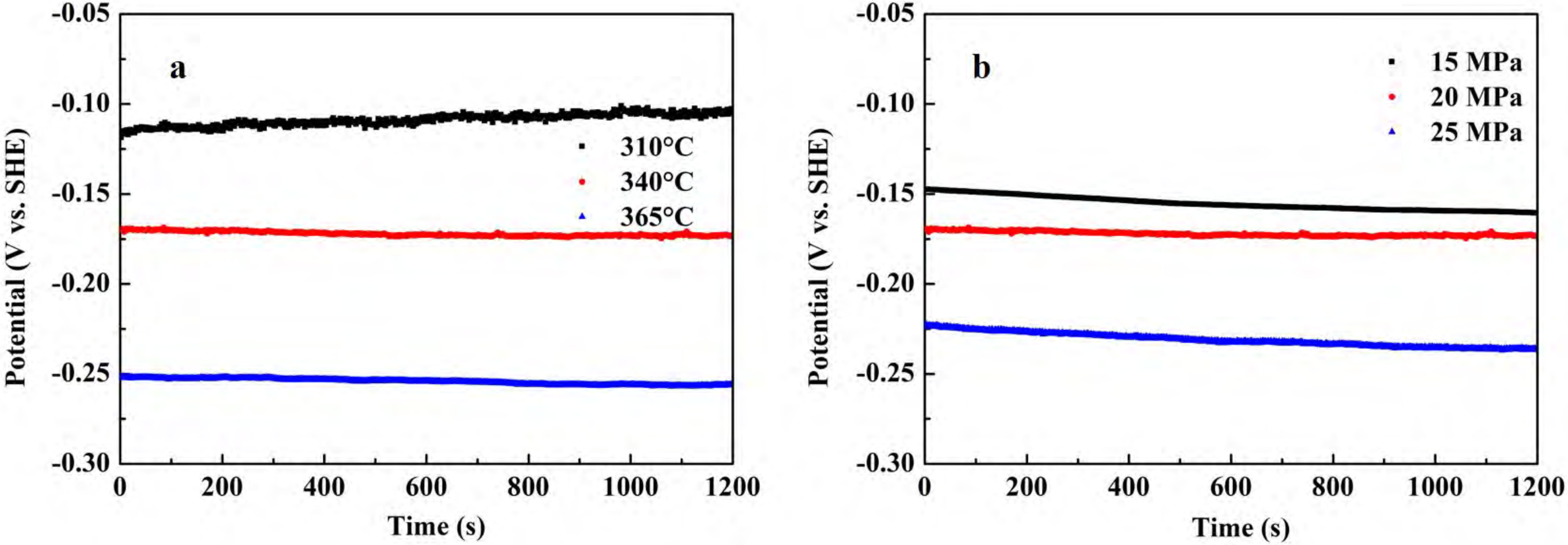
a
310°C
340°C
365°C
Potential (V vs. SHE)
Time (s)
-0.05
-0.10
-0.15
-0.20
-0.25
-0.30
0
200
400
600
800
1000
1200
b
15 MPa
20 MPa
25 MPa
Potential (V vs. SHE)
Time (s)

Figure 4

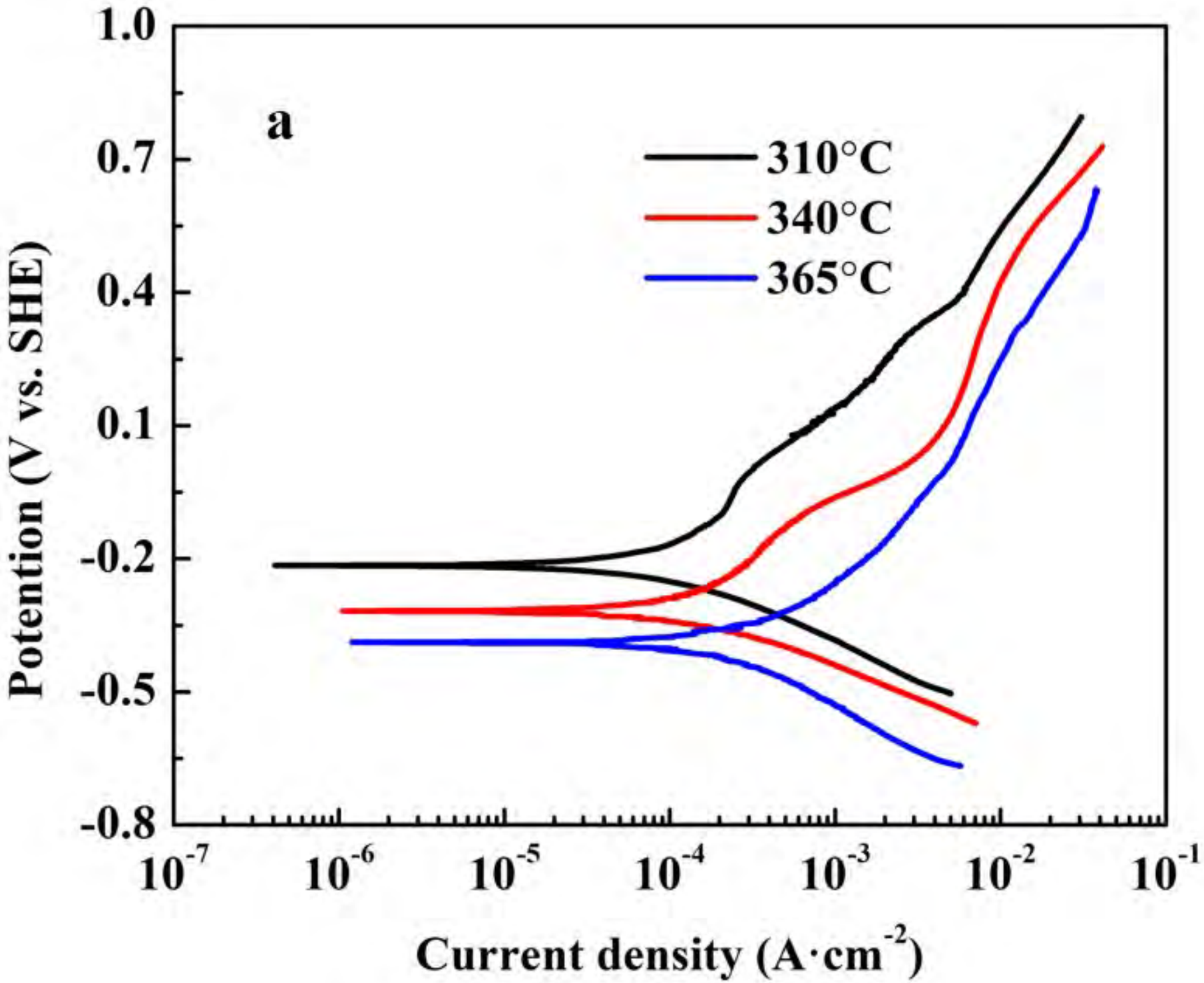
a
b
310°C
340°C
365°C
1.0
0.7
0.4
0.1
-0.2
-0.5
-0.8
Potention (V vs. SHE)
10^-7
10^-6
10^-5
10^-4
10^-3
10^-2
10^-1
Current density (A·cm^-2)

Figure 5

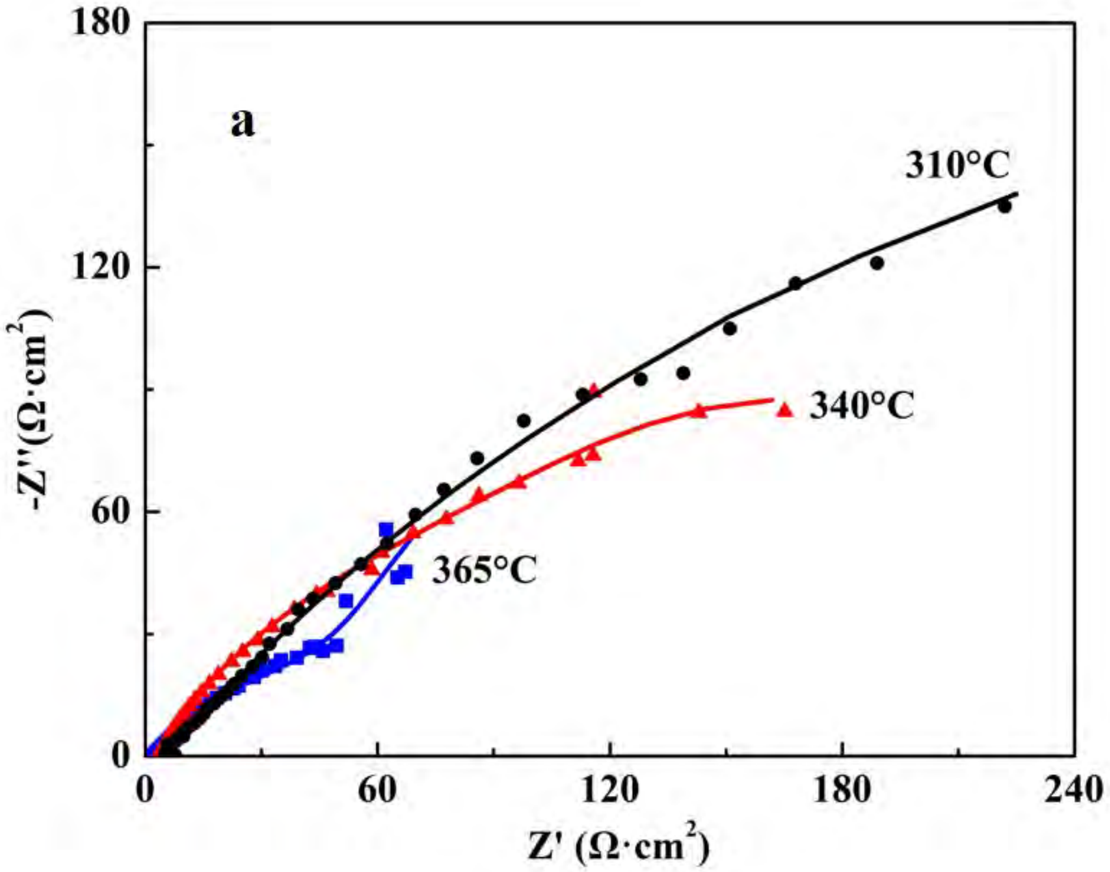
a
310°C
340°C
365°C
-Z''(Ω·cm²)
Z' (Ω·cm²)
0
60
120
180
240

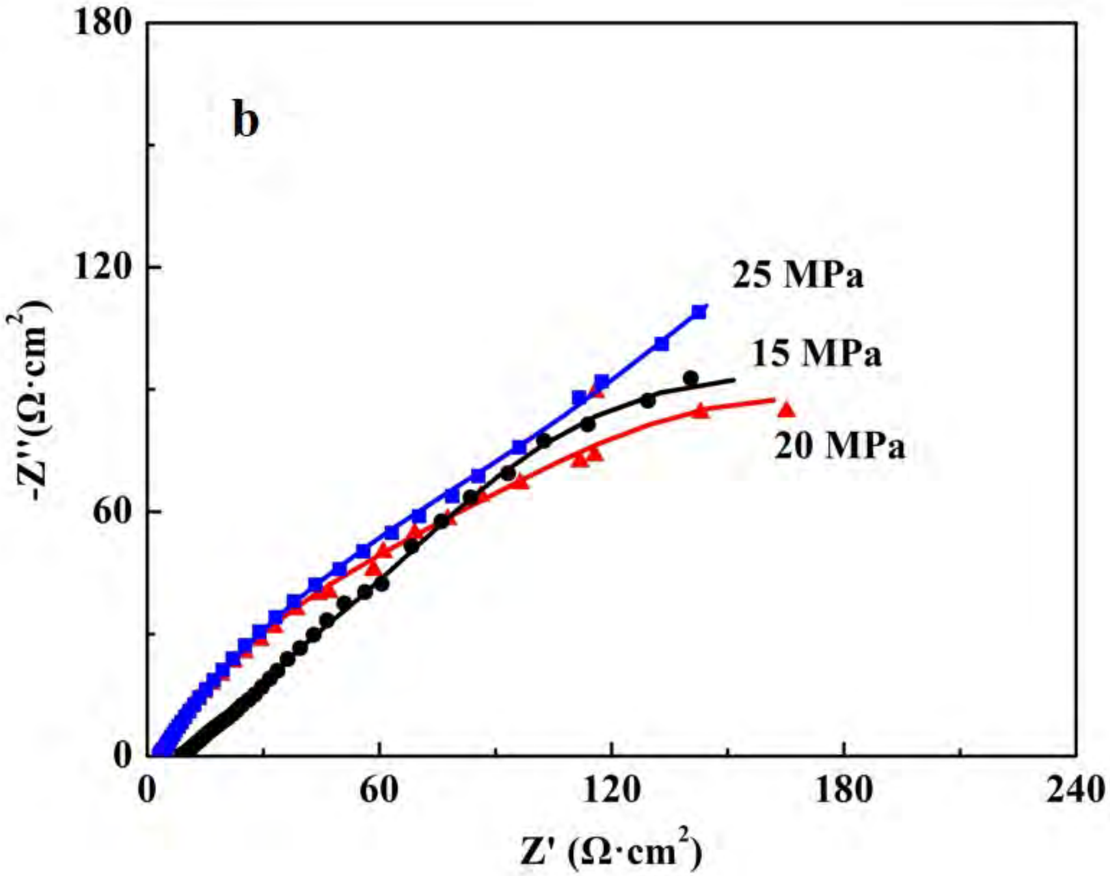
b
25 MPa
15 MPa
20 MPa
-Z''(Ω·cm²)
Z' (Ω·cm²)
0
60
120
180
240

Figure 6